

This is an Open Access document downloaded from ORCA, Cardiff University's institutional repository: <https://orca.cardiff.ac.uk/id/eprint/136936/>

This is the author's version of a work that was submitted to / accepted for publication.

Citation for final published version:

Sarma, Plaban Jyoti, Dowerah, Dikshita, Gour, Nand Kishor, Logsdail, Andrew J. , Catlow, C. Richard A. and Deka, Ramesh 2021. Tuning the transition barrier of H₂ dissociation in the hydrogenation of CO₂ to formic acid on Ti-doped Sn₂O₄ cluster. *Physical Chemistry Chemical Physics* 23 (1) , pp. 204-210. 10.1039/D0CP04472E

Publishers page: <http://dx.doi.org/10.1039/D0CP04472E>

Please note:

Changes made as a result of publishing processes such as copy-editing, formatting and page numbers may not be reflected in this version. For the definitive version of this publication, please refer to the published source. You are advised to consult the publisher's version if you wish to cite this paper.

This version is being made available in accordance with publisher policies. See <http://orca.cf.ac.uk/policies.html> for usage policies. Copyright and moral rights for publications made available in ORCA are retained by the copyright holders.



Tuning the transition barrier of H₂ dissociation in the hydrogenation of CO₂ to formic acid on Ti-doped Sn₂O₄ cluster

Plaban J. Sarma¹, Dikshita Dowerah¹, Nand K. Gour¹, Andrew J. Logsdail², C. Richard A. Catlow^{2,3,4} and Ramesh Ch. Deka*¹

¹Department of Chemical Sciences, Tezpur University, Tezpur, Assam, India

²Cardiff Catalysis Institute, School of Chemistry, Cardiff University, Cardiff CF10 3AT, UK

³Department of Chemistry, University College London, 20 Gordon St., London WC1HOAJ, UK

⁴UK Catalysis Hub, Research Complex at Harwell, RAL, Oxford, OX11 0FA, UK

E-mail: ramesh@tezu.ernet.in

Abstract

Titanium doped Sn₂O₄ cluster shows robust catalytic activity for selective CO₂ reduction from density functional theory study. Our study focuses on the importance of small sized clusters in catalytic reduction of CO₂ at lower overpotential. We investigate the influence of dopants on the height of the H₂ dissociation barrier on the doped systems, and then the subsequent mechanism for the conversion of CO₂ into formic acid (FA) via a hydride pinning pathway. The lowest barrier height for H₂ dissociation is observed across the 'Ti-O' bond of the Ti-doped Sn₂O₄ cluster, with a negatively charged hydride (Ti-H) formed during the heterolytic H₂ dissociation, bringing selectivity towards the desired FA product. The formation of a formate intermediate is identified as the rate determining step (RDS) for the whole pathway, but the barrier height is substantially reduced for the Ti-doped system when compared to the same steps on the undoped Sn₂O₄ cluster. The free energy of formate formation in the RDS is calculated to be negative, which reveals that the hydride transfer would occur spontaneously. Overall, our results show that small sized Ti-doped Sn₂O₄ clusters exhibit better catalytic activity than undoped clusters in the important process of reducing CO₂ to FA when proceeding via the hydride pinning pathway.

Keywords: Ti-doping, H₂-dissociation, CO₂ hydrogenation, formic acid, hydride-pathway.

Introduction

Combustion of fossil fuels is a major contributing factor to the increasing atmospheric concentration of CO₂, which is regarded as one of the major anthropogenic contributors to global warming.^{1,2} To address the current “Climate Emergency”, mitigation of CO₂ either by conversion or trapping is now essential. For this purpose, reduction of CO₂ into commercial valuable chemicals such as formic acid (FA), methanol and longer chained alcohols is highly advantageous.³⁻⁵ Furthermore, hydrogenation of CO₂ to liquid phase HCOOH and CH₃OH also addresses challenges associated with storage and transport of H₂, with the low volumetric density of H₂ in gas phase considered prohibitive for its potential use as an energy vector; HCOOH is a non-toxic liquid at room temperature, making it easy to transport and allowing direct implementation in fuel cells.⁶ Currently, however, chemical reduction of CO₂ to formic acid is limited by the availability of suitable catalysts to activate the thermodynamically stable C=O bond, which has a bond energy of 5.52 eV (533 kJ mol⁻¹).⁷ There are several reported methods of CO₂ reduction, including catalytic hydrogenation, electrochemical reduction, photocatalysis and biological reduction; among these, electrochemical and photochemical reduction are promising for facilitating product selectivity, lower production costs and high catalytic efficiency.⁸⁻¹⁰

During the last decade, the study of Sn-based electrodes for electrochemical CO₂ reduction has grown rapidly due to the higher overpotentials necessary for competing H₂ evolution reactions, thus bringing selectivity to the reduction of CO₂ to HCOOH.¹¹⁻¹³ Like other non-noble metals, tin undergoes corrosion and degradation, but the oxide layer formed has been identified as highly catalytic towards the electrochemical reduction of CO₂. The importance of the oxide layer was highlighted by Chen and Kanan, who reported that the catalytic activity of SnO₂ depends on the oxide layer percentage, showing that the depth of the oxide layer was proportional to the reduction efficiency.¹⁴ Particle size effects also have an important effect on catalyst efficacy, with Xu *et al.* describing the significance of quantum confinement for SnO₂ quantum dots (QDs) within the range of 0.5-2.5 nm, as illustrated for gas sensing properties towards ethanol; QDs show higher sensitivity than larger SnO₂ nanowires.¹⁵ Liu *et al.* compared the electrocatalytic properties of SnO₂ quantum wires (1.7 nm) with SnO₂ nanoparticles (5.5 nm) for HCOOH formation and concluded that the quantum wires have exposed grain boundaries that enhance the current density, as well as Faradic efficiency, by over 80% for HCOOH formation.¹⁶ This also reveals the

importance of small sized clusters in the catalytic reduction of CO₂ to HCOOH and it influences the overpotential of formic acid production.

In contrast to the catalytic application of pure SnO₂ clusters, there is limited literature for the application of doped SnO₂ clusters towards the hydrogenation of CO₂ to HCOOH. H₂ dissociation on doped metal oxide clusters and surfaces such as Al-doped ZnO, CeO₂ and MgO have been reported, as well as on Ni clusters doped with Rh, Pt, Pd and Au metals;^{17,18} However, the mechanism of CO₂ reduction using doped-SnO₂ nanoparticles remains relatively unexplored. Saravanan *et al.* performed theoretical calculations of SnO₂ surfaces to try and understand the consequences of transition metal doping,¹⁹ considering two types of dopants: Ti, V, Nb, Ta and Zr replacing the six coordinated Sn(IV) in a pristine crystal; and Cd, Co, Pb, Sb and Zn accompanied by a neighbouring O vacancy, i.e. at an Sn(II) site. The extrinsic dopants at the Sn(IV) site resulted in a material showing potential to reduce CO₂ to HCOOH at lower overpotentials than pure SnO₂, with Ti-doped SnO₂ identified as the best catalyst. Such Ti-doped SnO₂ nanoparticles are used currently as sensing materials for ethanol, and both Ti- and Si-doped SnO₂ nanoparticles have been studied to understand the influence of the doping metal on the electrical conductivity.²⁰⁻²²⁻

Previously, CO₂ activation on the catalyst surface has been reported as occurring by the formation of a carbonate-like structure, followed by the transfer of a hydrogen atom to the carbon atom, producing formate and subsequently formic acid.^{14,23,24} Earlier studies show that H₂ can dissociate heterolytically on ZnO clusters, which leads to the formation of a metal-hydride bond.^{17,25} Similarly, another study on SnO₂ reported a hydride pinning pathway whereby heterolytic H₂ dissociation leads to the formation of an Sn-hydride bond, and CO₂ activation occurs during the (rate determining) hydride transfer step; The observed outcome was total selectivity of HCOOH formation at an overpotential of 0.25 eV.²⁶ In the present work, we consider whether dopants in a model dimeric Sn₂O₄ cluster modify the key steps in this favourable hydrogenation pathway of CO₂ to HCOOH. Structures for the Sn₂O₄ clusters have been taken from previous studies²⁶ and, for the newly considered doped system, we choose two dopants: Si, which is isovalent with Sn, with a stable +4 oxidation state as well as vacant 3d orbitals; and Ti, which has an atomic radius similar to Sn, vacant 3d electrons, and stability in the +4 oxidation state (though somewhat reducible). As both dopants are considered formally in +4 oxidation states, their introduction to the cluster does not require compensating oxygen vacancies.

Results and discussion

Structures of Si and Ti-doped Sn₂O₄ cluster.

Si and Ti dopants replace an Sn atom in the small dimeric Sn₂O₄ cluster, and the structures were geometry optimized using DFT (Fig. 1). The structure of the SnSiO₄ cluster is similar to that of the pure Sn₂O₄ cluster, maintaining a planar 2-dimensional configuration; in contrast, the SnTiO₄ cluster is 3-dimensional, with the Ti-center taking a distorted T_d shape surrounded by two bridging and one terminal oxygen. The shape of the TiO₃ unit in the SnTiO₄ cluster resembles the Ti-center of a pure Ti₂O₄ cluster.²⁷

The formation energy (E_f) of the doped clusters upon replacement of one Sn by the Si or Ti atom is calculated via the equation as follows:

$$E_f = (E_{SnMO_4} + E_{SnO_2}) - (E_{Sn_2O_4} + E_{MO_2}),$$

where M corresponds to the dopant Si or Ti species. The formation energy of the SnSiO₄ and SnTiO₄ clusters with respect to the Sn₂O₄ and MO₂ (SiO₂ and TiO₂) clusters are calculated to be -0.80 eV (-18.55 kcal/mol) and -0.73 eV (-16.83 kcal/mol) respectively, indicating that doping of these small clusters is thermodynamically feasible. SnSiO₄ has a lower energy than SnTiO₄, due to the greater strength of the Si-O bond.²⁸

Natural bond orbital (NBO) calculations have been performed to interpret the bonding interactions of the metal dopants with the oxygen atoms in the clusters, and diagrams of the highest occupied molecular orbital (HOMO) and lowest unoccupied molecular orbital (LUMO) are included accordingly in Fig. 1. HOMOs of both of the doped clusters are concentrated on the lone pairs of oxygen, i.e. the non-bonding electrons. The LUMO of SnSiO₄ has the π^* character of an O-Si bond, and some character on the Sn-center, which provides us the evidence of having O-Si π interaction resulting from the back donation of electron density from the oxygen lone pairs to the empty 3d orbitals of silicon. To verify the involvement of Si d orbitals in the bonding interactions, we have analyzed the percentage of individual atomic contributions towards the participating bonds in the SnSiO₄ and SnTiO₄ clusters (Table1, column 4), along with the orbital contributions of the s, p and d orbitals (Table1, column 5). Some occupancy of the Si d orbitals is observed in both the terminal and bridging Si-O bonds, along with the s and p orbitals, which reveals the O-Si

π bonding interaction includes the contributions from the Si d orbitals; however, for the SnTiO₄ cluster, the percentage contribution of the d orbitals is much more than the s and p orbitals. These

observations lead us to conclude that the more stable covalent-like Si interactions in the SnSiO₄ cluster favourably stabilise the system when compared to the Ti-dopant in SnTiO₄. The individual atomic contributions (column 4) of the participating bonds shows that O contributes significantly in bonding compared to the Sn, Si and Ti atoms.

Table 1: Percentage contribution of orbitals to the bridging and terminal metal-oxygen bonds as calculated via an NBO calculation at the MN12-SX/def2TZVPP level of theory.

Cluster	Bond type	Atom	Elemental Contribution (%)	Angular Contribution (%)
SnSiO ₄	Bridging Si-O	Si	12.65	s (27.98) p (48.21) d (23.78)
		O	87.35	s (33.69) p (65.90)
	Terminal Si-O	Si	19.53	s (43.39) p (55.60) d (0.99)
		O	80.47	s (34.36) p (65.0%)
	Bridging Sn-O	Sn	12.82	s (26.54) p (72.66) d (0.45)
		O	87.18	s (12.24) p (87.36)
	Terminal Sn-O	Sn	29.85	s (46.92) p (52.58) d (0.33)
		O	70.15	s (6.94) p (92.93)
SnTiO ₄	Bridging Ti-O	Ti	12.86	s (23.60) p (23.94) d (51.79)
		O	87.14	s (29.51) p (70.39)
	Terminal Ti-O	Ti	20.57	s (10.69) p (7.40) d (81.33)
		O	79.43	s (19.70) p (80.22)
	Bridging Sn-O	Sn	13.65	s (27.35) p (71.28) d (0.89)
		O	86.35	s (9.23) p (90.65)
	Terminal Sn-O	Sn	28.95	s (45.08) p (54.31) d (0.43)
		O	71.05	s (7.29) p (92.58)

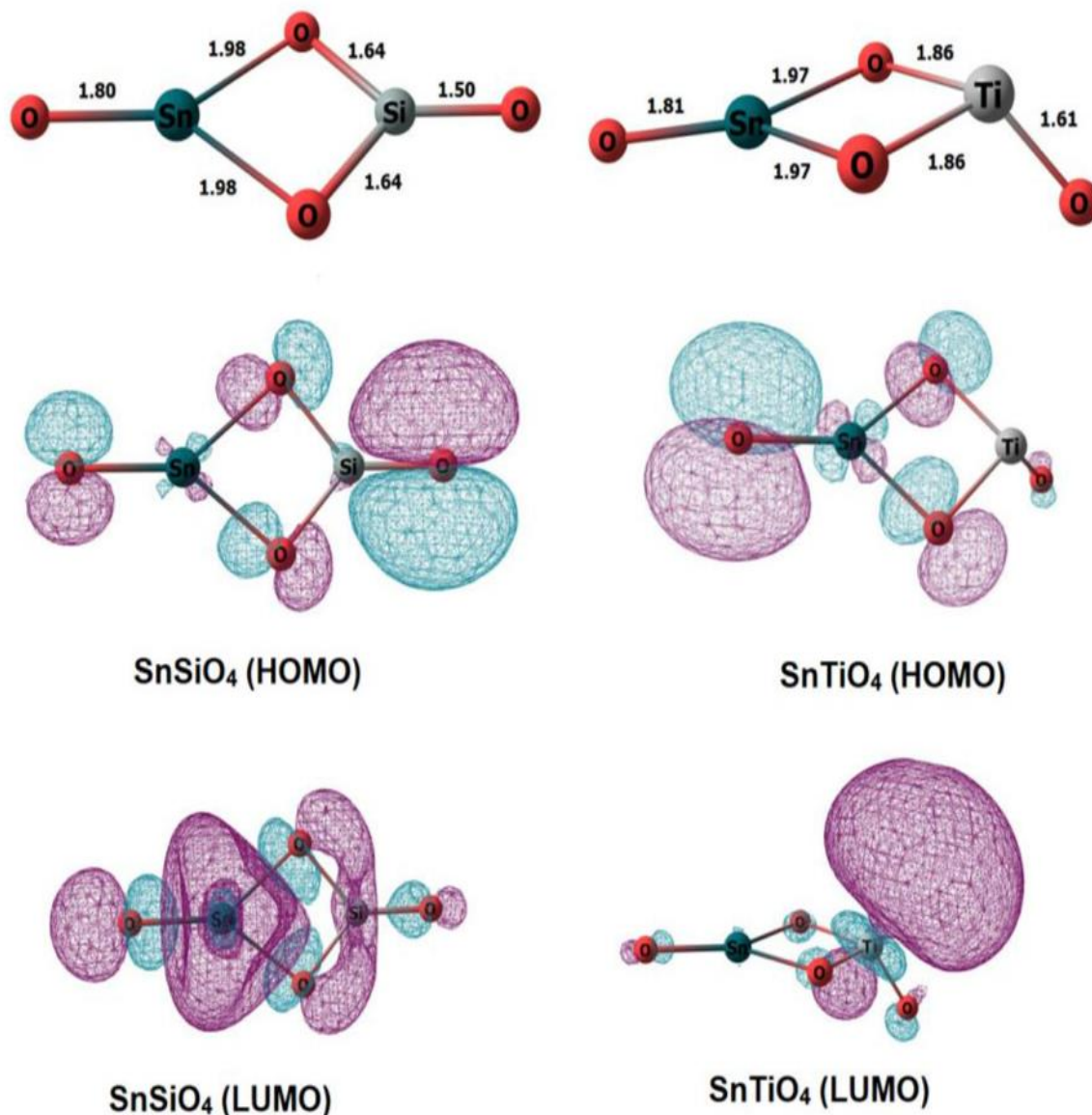


Fig. 1 Optimized geometries of SnSiO_4 (left) and SnTiO_4 (right) clusters, along with HOMO and LUMO, as calculated at the MN12-SX/def2tzvpp level of theory. The different colours (aqua/magenta) of the orbitals indicate the phases of the orbitals taken at the cutoff of 0.03.

H₂ dissociation on the SnMO_4 clusters

Previously, undoped Sn_2O_4 clusters have been observed to dissociate H_2 at Sn-O bridging sites, with the hydride pinning pathway leading to selective reduction of CO_2 to HCOOH via a formate intermediate.²⁶ Considering this previous work, we calculated the transition states and barrier heights of H_2 dissociation on all possible bridging sites in the doped cluster; the subsequent

optimized minima and transition state geometries are shown in Fig. 2, and the reaction energy profiles in Fig. 3.

For the SnSiO_4 cluster, the activation energy for H_2 dissociation is 1.76 eV (40.61 kcal/mol) on a Si-O bond, which is 0.26 eV (5.99 kcal/mol) higher than at the Sn-O bond [1.50 eV, 34.73 kcal/mol]. The transition states corresponding to H_2 dissociation on Si-O (A-B) and Sn-O (A-B') sites (Fig. 2) are characterized by the presence of imaginary frequency of $1524i \text{ cm}^{-1}$ and $1438i \text{ cm}^{-1}$, respectively. The dissociated products 'B' and 'B'', formed on the Si-O and Sn-O sites, respectively, are also shown in Fig. 2. Interestingly, despite dissociation occurring at the bridging position of the Si-O site for product B, as confirmed via the transition state (A-B) and IRC calculation (Fig. S1), the product has a geometry based on the terminal Si-O bond. The convergence graph is shown in Fig. 4 for the reaction $\text{A} \rightarrow \text{A-B} \rightarrow \text{B}$. Fig. 4 indicates that, whilst the H_2 dissociation transition state is at the bridging site, the product H is unstable at this bridging location and converts to a more stable terminal-positioned structure (Fig. 2, structure B). We attribute the formation of the terminal H to the Si-O $d\pi$ - $p\pi$ interaction observed for the bridging Si-O bond in the SnSiO_4 cluster, which provides extra stability to the bridging Si-O bonds; the $d\pi$ - $p\pi$ interaction is less pronounced in the terminal Si-O bond, with the contribution of the Si d orbital reduced (0.99%, compared to 23.78% for the bridging bond). The H_2 dissociation on the Sn-O site results in similar structural arrangement to H_2 dissociation on the undoped Sn_2O_4 cluster investigated previously.²⁶

In contrast, the SnTiO_4 cluster shows a smaller barrier on the Ti-O bridge (C-D) of 0.98 eV (22.62 kcal/mol), with an imaginary frequency of $1373i \text{ cm}^{-1}$. The barrier height is 0.50 eV (11.68 kcal/mol) lower than that of Sn-O bridge (C-D'), as shown in Fig. 3. The lower barrier over the Ti-O bridge can be explained via the orbital structures: The LUMO of the SnTiO_4 cluster is located on the Ti-center and thus, when H_2 dissociation takes place over Ti-O bridge, it occurs via interaction with the LUMO; However, on the Sn-O bridge, H_2 dissociation cannot take place through the Ti-centered LUMO, interacting instead with the LUMO+1 (Fig. S2). Therefore, a higher orbital reorganization energy is required for H_2 dissociation over the Sn-O bridge, which leads to a larger activation energy for the process. Notably, H_2 dissociation on the Ti-O site has a lower activation energy than on the Sn-O site in doped and undoped Sn_2O_4 cluster (barrier height = 1.25 eV).²⁶

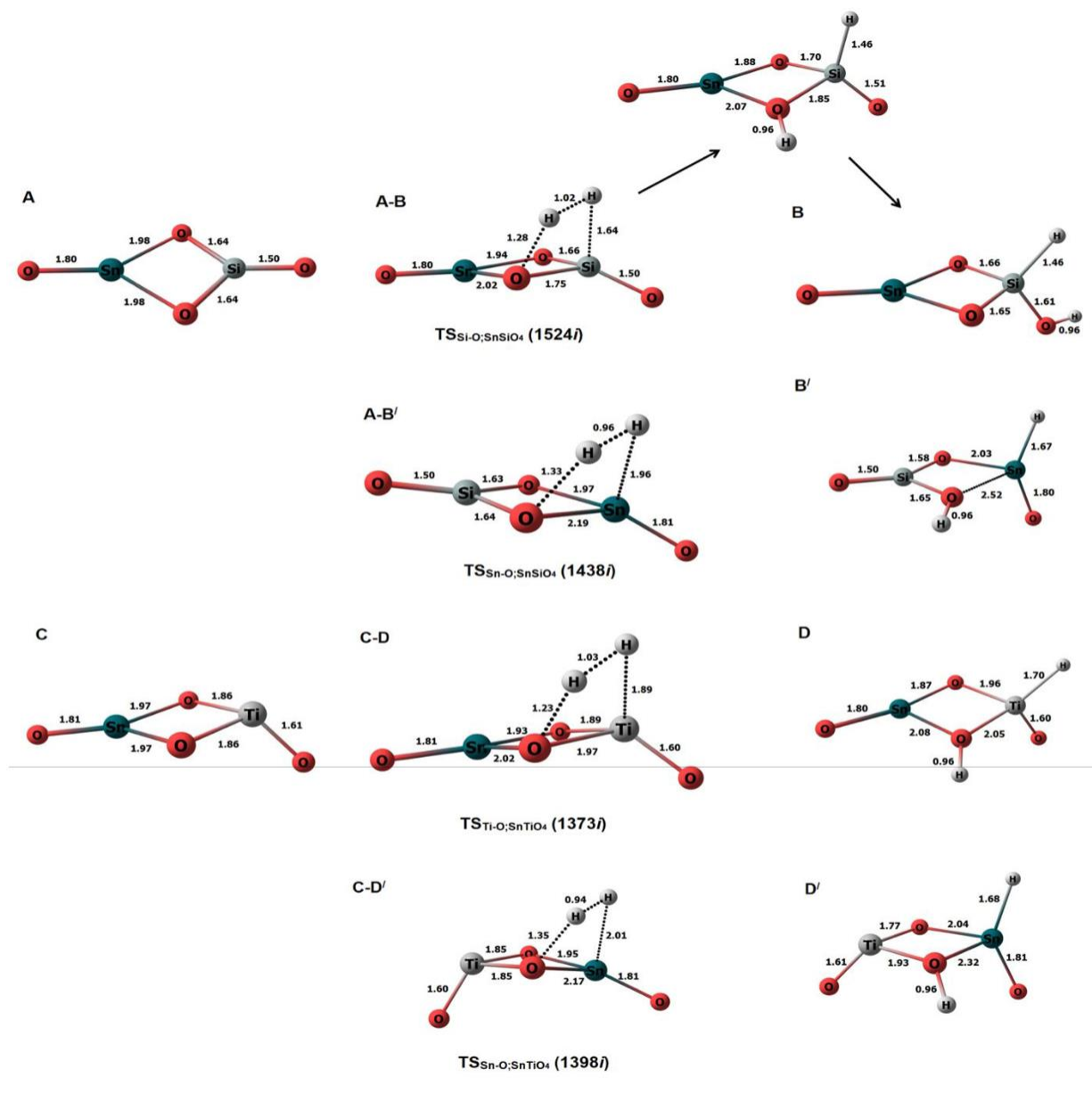


Fig. 2 The optimized structures of doped clusters along with the transition states and H₂ dissociated products: Top: SnSiO₄; Bottom: SnTiO₄.

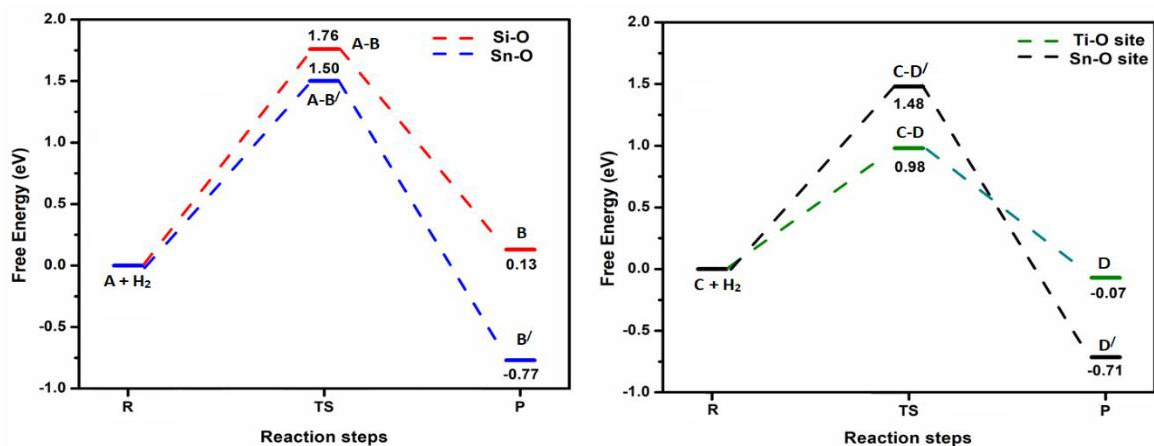


Fig. 3 The potential energy profile diagram comparing the dissociation of H₂ on the ‘Sn-O’ and ‘M-O’ site of the SnSiO₄ (left) and SnTiO₄ (right) clusters, calculated at the MN12-SX/def2tzvpp level of theory.

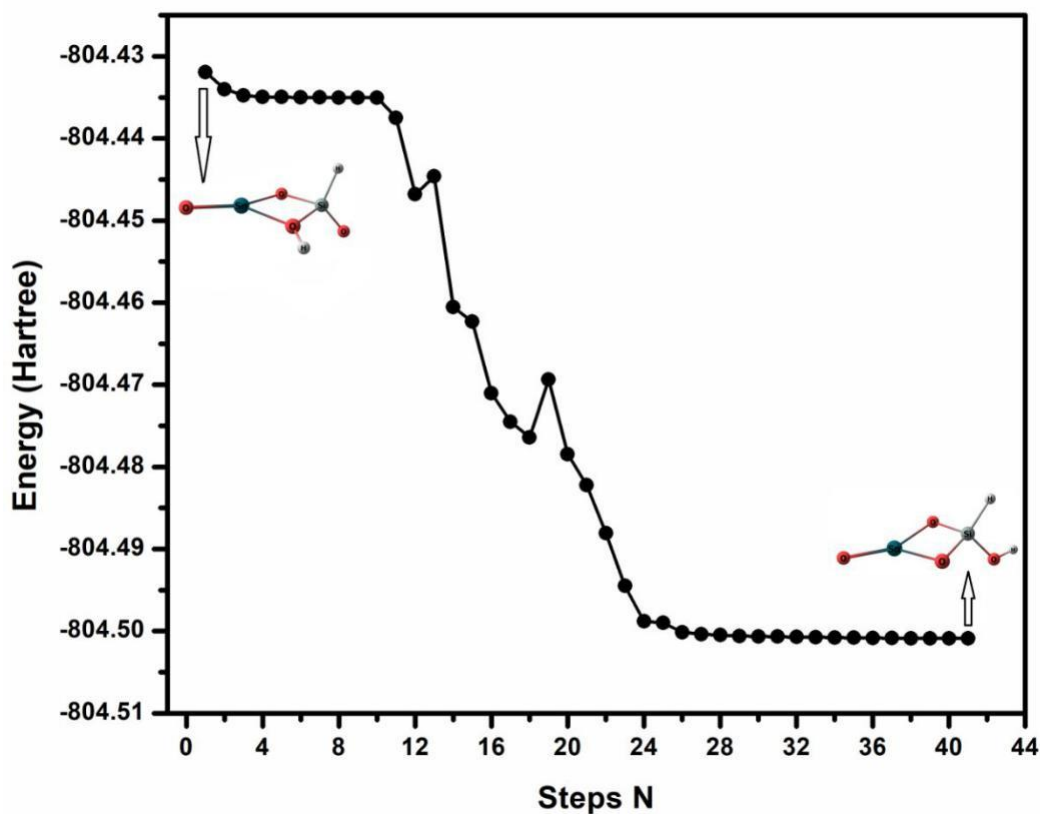


Fig. 4 Structural convergence from H₂ dissociation at bridging ‘Si-O’ site to terminal ‘Si-O’ site.

To understand the strength of the M-H bond, and confirm whether the hydride ion has formed, we analyzed the Bader charge of the H₂ dissociated products (B, B', D & D') in Table 2. A hydride is observed in all the models, as the hydrogen of newly formed M-H possesses a negative

formal charge. The calculated percentage of orbital contribution of H and M in the M-H bond are shown in Table 3; in the bonding of Si-H, the contribution of the Si 3p orbital is greatest (46.86%), whereas the Ti-H bond is formed most prominently of 3d orbitals (44.90%). In the latter case, the contribution of d is more than valence 4s and 4p orbitals, which contribute 25.81% and 29.12%, respectively, and as a consequence the Ti-H bond is weaker than the Si-H.

Table 2. Bader charges and bond distance of reacting atoms on all sites of the doped clusters.

Structure	Bond	Bond distance, Å	Bader charges, e
B	Si-H	1.46	Si = +3.15, H = -0.71
	O-H	0.96	O = -1.45, H = +0.70
B/	Sn-H	1.67	Sn = +1.98, H = -0.25
	O-H	0.96	O = -1.53, H = +0.70
D	Ti-H	1.60	Ti = +2.17, H = -0.55
	O-H	0.96	O = -1.37, H = +0.68
D/	Sn-H	1.67	Sn = +1.99, H = -0.27
	O-H	0.96	O = -1.36, H = +0.67

Table 3. Percentage of orbital contribution of all metal-hydride bonds obtained via NBO calculation performed at MN12-SX/def2TZVPP level of theory.

Cluster	Atom	Elemental Contribution (%)	Angular Contribution (%)
SnSiO ₄	Si	31.60	s (30.85)p (46.86) d (22.21)
	H	68.40	s (99.93) p (0.07)
	Sn	37.57	s (31.12) p (68.44) d (0.33)
	H	62.43	s (99.85) p (0.14)
SnTiO ₄	Ti	36.88	s (25.81)p (29.12) d (44.90)
	H	63.12	s (99.85) p (0.14)
	Sn	38.10	s (42.59) p (56.78) d (0.56)
	H	61.90	s (99.86) p (0.14)

Mechanistic study via hydride pinning pathway

After dissociation of H₂ on the doped Sn₂O₄ cluster, we extended our study to the hydrogenation of CO₂ via the hydride pinning pathway. As already discussed, the H₂ dissociation barrier height is lower on SnTiO₄ than SnSiO₄, and hence CO₂ reduction is considered only on the SnTiO₄ cluster. The overall pathway follows a two-step catalytic mechanism:²⁶

- a) First, gas phase CO₂ takes up the hydride from the catalytic site following the ‘Eley Rideal’ (ER) mechanism and binds with the Sn-center in the cluster.
- b) Second, the remaining hydrogen transfers to the co-adsorbed oxygen of HCOO by following a ‘Langmuir Hinshelwood’ (LH) mechanism, to form the product HCOOH.

The potential energy pathway for hydrogenation of CO₂ on the SnTiO₄ cluster is presented in Fig. 5. In the mechanism studied, the hydride pinning step is initiated by the product ‘D’ (Fig. 2) where the hydride is transferred from the Ti-site to the carbon of CO₂ to form the formate (HCOO*) intermediate that further binds with the catalyst by one of the intermediate’s oxygens. This hydride transfer step proceeds via a transition state TS1 (607i cm⁻¹) to form the intermediate IM2 with an activation energy of 0.49 eV (11.49 kcal/mol). The transition barrier of the hydride transfer step in the doped system is lower than for the undoped cluster [1.15 eV (26.51 kcal/mol)],²⁶ which is attributed to the two factors: first, the weakness of the Ti-H bond relative to the Sn-H bond, which results in hydride transfer to the carbon being less energetically demanding; second, the Ti-centre in the doped SnTiO₄ cluster retains its tetrahedral shape throughout *i.e* energy is not required for structure changes of SnTiO₄, unlike for bare Sn₂O₄ where the Sn-centre changes its shape from tetrahedral to planar.²⁶ In the transition state TS1, the Ti-H bond elongates from 1.60 Å to 1.78 Å, while the bond distance of the newly formed C-H and Sn-O are 1.73 Å and 2.33 Å, respectively. After the formation of the HCOO* intermediate, the orientation spontaneously changes to IM2’ by flipping the -CHO group of HCOO* around the C-O(-Sn) bond, with a ΔG of -0.30 eV (-6.91 kcal/mol), which then allows uptake of the second hydrogen from the cluster. In the optimized IM2’, we observe a new Sn...O interaction of 2.36 Å (along with the remaining Sn-O bond); the O is now nearer to the remaining H on the cluster, and this hydrogen then transfers from the cluster to form HCOOH. During the formation of HCOOH, IM2’ overcomes an activation barrier of 0.35 eV (8.17 kcal/mol) via the transition state TS2 (920i cm⁻¹), which is smaller than the pinning step (TS1) and so indicating the reaction will proceed rapidly to the equilibrium once

the HCOO^* intermediate is formed. The HCOOH product leaves the catalytic cycle in the same step and hence the catalyst is recycled for the next H_2 dissociation step.

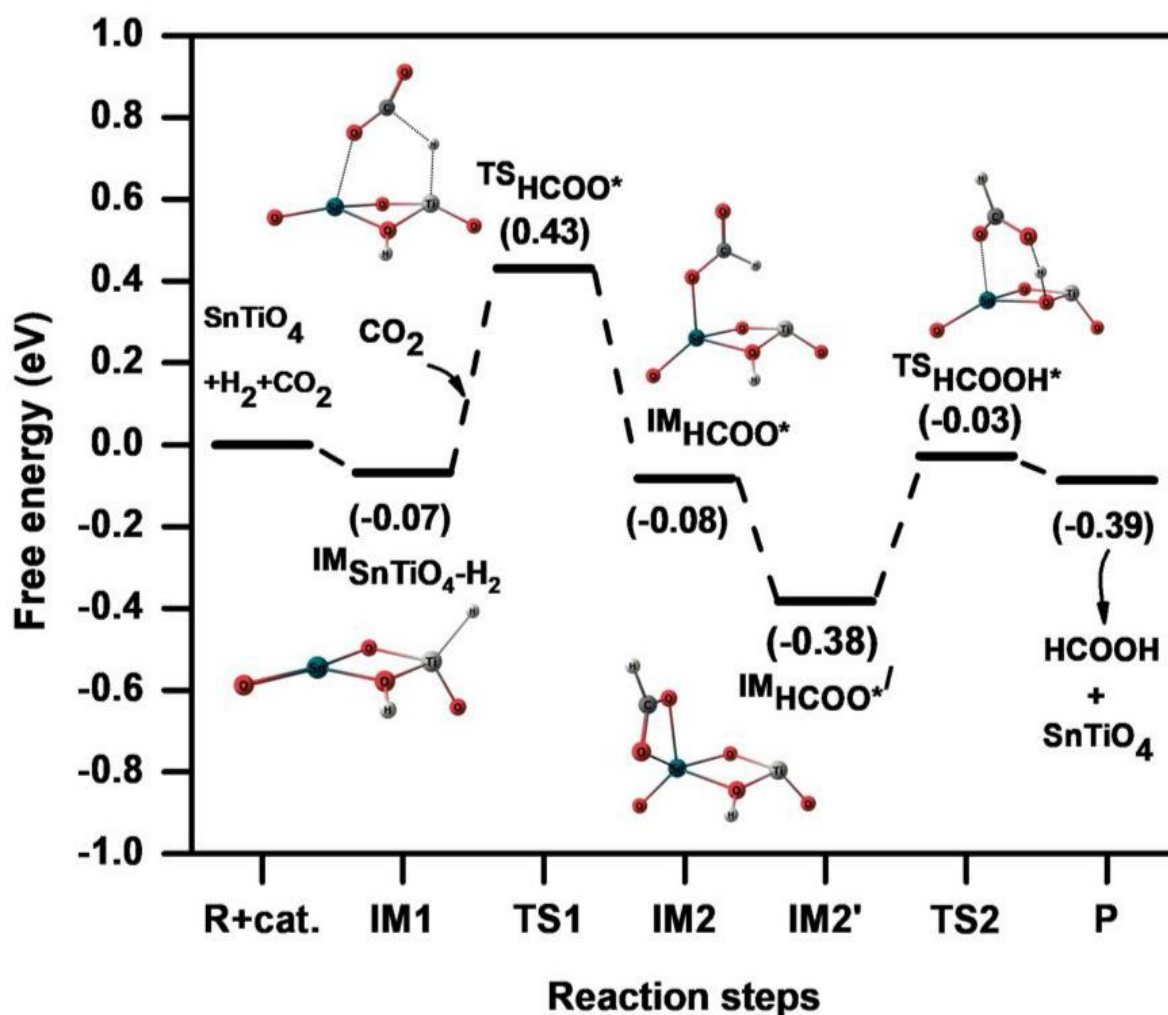


Fig. 5 Potential energy diagram representing the hydrogenation of CO_2 to HCOOH on SnTiO_4 cluster via hydride pinning pathway.

For the overall reaction, the hydride pinning step (TS1) is the rate-determining step (RDS) and hence the free energy difference between $\text{IM2}'$ and IM1 equates to the necessary overpotential for realising the hydrogenation process. This overpotential factor can be calculated from the computational hydrogen electrode (CHE) model given by Nørskov *et al.*,³⁷ which is discussed in the computational methodology. In the outlined reaction mechanism, the difference in free energies is -0.31 eV, which reveals the formation of HCOO^* intermediate is calculated to be

thermodynamically spontaneous. This spontaneity was not observed in the case of undoped Sn_2O_4 , where the required overpotential of HCOO^* formation is 0.25 eV.²⁶

Comparing the present results with previous studies on the hydrogenation of CO_2 to HCOOH on dimeric SnO_2 ,²⁶ we can propose the following:

- a) The H_2 dissociation barrier height on the Ti-doped Sn_2O_4 is 0.98 eV, which is 0.54 eV lower than the undoped Sn_2O_4 (1.52 eV). The doped cluster is therefore a potentially more active catalyst due to the reduced kinetic H_2 dissociation barrier.
- b) In the hydride transfer step, the barrier height for formate formation is 0.49 eV on the Ti-doped cluster, which is 0.66 eV greater than the undoped Sn_2O_4 (1.15 eV). The doped cluster therefore has potentially improved catalytic selectivity towards reduction of CO_2 to HCOOH via the hydride pinning pathway.
- c) Lastly, the overpotential factor drops from 0.25 eV when using the undoped Sn_2O_4 cluster to -0.31 eV for SnTiO_4 , correlating with the previous work reported by Saravanan *et al.*¹⁹ and illustrating that the reaction would proceed favourably.

Summary and Conclusions

Titanium and silicon dopants have been considered on the Sn^{4+} centers of a pure Sn_2O_4 cluster, and subsequently tested in the context of CO_2 hydrogenation. Negative formation energies for SnSiO_4 and SnTiO_4 reveal the replacement of Sn by Si or Ti to be energetically favourable. H_2 dissociation barrier heights are calculated as favourable on all the bridging sites available on the clusters, with the lowest activation energy on the bridging Ti-O site of the SnTiO_4 cluster. Our observations of the potential role for Si and Ti dopants informs that metals providing π character in the M-O bond will be less suitable catalysts for CO_2 reduction, while first and second row early transition metals (e.g. Ti, V, Nb and Zr), are good candidates as dopants in SnO_2 clusters because π bonding is less common. Bader charge analysis of the metal-hydride (Ti-H) shows that one H on each cluster possesses a formal negative charge. The hydride is key in the hydride assisted pathways for CO_2 reduction, triggering the total selectivity for the formation of HCOOH over CO at lower overpotential. The SnTiO_4 cluster has a reduced barrier relative to the pure Sn_2O_4 cluster in the rate-determining step (HCOO^* formation), and also requires a lower overpotential for the formation of HCOOH , delivering product selectivity. Experimentally, small sized bare SnO_2

quantum dots are used for the conversion of CO₂ to HCOOH at low overpotentials but use of Ti-doped SnO₂ particles is not yet reported; Therefore, our results should be considered as a stimulus for further experimental investigation of HCOOH formation via the hydride pinning pathway.

Methodology

Kohn-Sham density functional theory (DFT), as implemented in the Gaussian 09 software package,²⁹ has been used to obtain the lowest energy structures and thermo-chemical properties involved in the mechanism of CO₂ reduction. For geometry relaxation and frequency calculations, a range-separated hybrid non-separable meta-NGA, MN12-SX,³⁰ is used; the accuracy of the MN12-SX density functional when predicting structures and energies has been extensively studied previously.^{26,31,32} A combination of density fitting triple- ξ def2TZVPP basis sets is used,³³ as these minimise the basis set superposition error (BSSE) and give results close to the DFT basis set limit;³⁴ the BSSE is < 0.04 eV with the triple- ξ basis set, and energies reported in the manuscript include this correction.

Frequency calculations are used to confirm the stability of the reactants (R), intermediates (IM) and products (P) along the reaction pathway, and to verify the transition states (TS) identified. The presence of one imaginary frequency, consistent with the eigenvector along with the reaction coordinate, confirms the TS structure is a first-order saddle point, whereas only real vibrational frequencies are observed for the R, IM and P minima. Changes in the free energy of each reaction steps (ΔG) and free energy of activation (ΔG^\ddagger) are calculated from the free energy difference between the final and initial states, assuming room temperature and atmospheric pressure (298 K, 1 atm). Formic acid is formed in the liquid phase at room temperature and therefore, as discussed elsewhere previously, a correction of -0.12 eV (taken from the NIST database) is included in our calculated energy of the FA product to account for the free energy difference between its liquid-and gas-phase forms.^{26,35} Bader charge analysis is performed on charge density distributions using the AIMALL software package.³⁶

To interpret the overpotential factor associated with the formic acid formation, we have used the computational hydrogen electrode (CHE) model, which correlates the reaction free energy change with the electrochemical potential. We calculate the free energy change at the rate-determining step (RDS), determined as the hydride transfer step to form the HCOO* intermediate, where the CHE gas-phase hydrogen is at equilibrium with a proton and electron pair ($H^+ + e^- \rightarrow$

1/2H₂) at a potential of 0 V against reversible hydrogen electrode (RHE) for all pH, all temperatures and 1 atm of pressure.³⁷

Conflicts of interest

There are no conflicts to declare.

Acknowledgement

The authors are thankful to Science & Engineering Research Board (SERB) (EMR/2016/003195), Department of Science and Technology (DST) nanomission ([SR/NM/NS-1147/2016(G)]) and Department of Biotechnology (DBT) project (BT/PR16182/NER/95/92/2015) New Delhi, India, and Tezpur university for financial support. The authors gratefully acknowledge Dr. Sanjeev P. Mahanta and Dr. Dharitri Das of Tezpur University for their valuable suggestions while carrying out the work.

References

1. J. C. Fyfe, N. P. Gillet and F. W. Zwiers, *Nat. Clim. Change*. 2013, 3, 767-769.
2. A. Stips, D. Macias, C. Coughlan, E. Garcia-Gorriz and X. S. Liang, *Sci. Rep.* 2016, 6, 21691-21699.
3. W. Li, H. Wang, X. Jiang, J. Zhu, Z. Liu, X. Guo and C. Song, *RSC adv.* 2018, 8, 7651-7669.
4. Q. Li, J. Fu, W. Zhu, Z. Chen, B. Shen, L. Wu, Z. Xi, T. Wang, G. Lu, J. Zhu and S. Sun, *J. Am. Chem. Soc.* 2017, 139, 4290-4293.
5. A. Álvarez, A. Bansode, A. Urakawa, A. V. Bavykina, T. A. Wezendonk, M. Makkee, J. Gascon and F. Kapteijn, *Chem. Rev.* 2017, 117, 9804-9838.
6. A.K. Singh, S. Singh and Kumar, *Catal. Sci.* 2016, 6, 12-40.
7. Ahmad, K.; Upadhyayula, S. *ENV progress and sustainable energy*. 2019, 38, 98-111.
8. Z. Sun, T. Ma, H. Tao, Q. Fan and B. Han, *Chem.* 2017, 3, 560-587.
9. F. Li, L. Chen, G. P. Knowles, D. R. MacFarlane and J. Zhang, *Angew. Chem - Int. Ed.* 2017, 56, 505-509.
10. J. Wu, Y. Huang, W. Ye and Y. Li, *Adv. Sci.* 2017, 4, 1-29.

11. J. Wu, F. G. Risalvato, S. Ma and X.D. Zhou, *J. Mater. Chem. A*. 2014, 2, 1647-1651.
12. W. Deng, L. Zhang, L. Li, S. Chen, C. Hu, Z.J. Zhao, T. Wang and J. Gong, *J. Am. Chem. Soc.* 2019, 141, 2911-2915.
13. S. Zhang, P. Kang and T.J. Meyer, *J. Am. Chem. Soc.* 2014, 136, 1734-1737.
14. Y. Chen and M. W. Kanan, *J. Am. Chem. Soc.* 2012, 134, 1986-1989.
15. X. Xu, J. Zhuang and X. Wang, *J. Am. Chem. Soc.* 2008, 130, 12527-12535.
16. S. Liu, J. Xiao, X.F. Lu, J. Wang, X. Wang and X.W. Lou, *Angew. Chem - Int. Ed.* 2019, 58, 8499-8503.
17. T.W. Keal, P. Sherwood, G. Dutta, A.A. Sokol and C.R.A. Catlow, *Proceedings of the Royal Society of London A: Mathematical, Physical and Engineering Sciences*. 2011, 467, 1900-1924.
18. N.S. Venkataramanan, A. Suvitha, H. Mizuseki and Y. Kawazoe, *Int. J. Quantum Chem.* 2013, 113, 1940-1948.
19. K. Saravanan, Y. Basdogan, J. Dean and J.A. Keith, *J. Mater. Chem. A*. 2017, 5, 11756-11763.
20. A. P. S. Isabel, C. H. Kao, R. K. Mahanty, Y. C. S. Wu, C. Y. Li, C. Y. Lin, and C. F. Lin, *Ceram. Int.* 2017, 43, 10386-10391.
21. J. Q. Wang, H. L. Kang and Y. Zhang, *Mater. Res. Express*. 2018, 5, 075902-075913.
22. J. Jang, H. Yim and J.W. Choi, *Thin Solid Films*. 2018, 660, 606-612.
23. Q. Tang, Y. Lee, D.Y. Li, W. Choi, C.W. Liu, D. Lee and D.E. Jiang, *J. Am. Chem. Soc.* 2017, 139, 9728-9736.
24. C.W. Lee, N.H. Cho, K.D. Yang and K.T. Nam, *ChemElectroChem*. 2017, 4, 2130-2136.
25. S.A. French, A.A. Sokol, S.T. Bromley, C.R.A. Catlow, S.C. Rogers, F. King and P. Sherwood, *Angew. Chem - Int. Ed.* 2001, 40, 4437-4440.
26. P. J. Sarma, S. D. Baruah, A. Logsdail and R. C. Deka, *ChemPhysChem*. 2019, 20, 680-686.
27. O. Lamiel-Garcia, A. Cuko, M. Calatayud, F. Illas and S.T. Bromley, *Nanoscale*. 2017, 9, 1049-1058.
28. F. Weinhold and R. West, *Organometallics*. 2011, 30, 5815-5824.
29. M. J. Frisch, G. W. Trucks, H. B. Schlegel, G. E. Scuseria, M. A. Robb, J. R. Cheeseman,

- G. Scalmani, V. Barone, B. Mennucci, G. A. Petersson, et al. Gaussian09 Revision D.01, Gaussian Inc. Wallingford CT. 2010.
30. R. Peverati and D. G. Truhlar, *Phys. Chem. Chem. Phys.* 2012, 14, 16187-16191.
 31. F. Weigend, *Phys. Chem. Chem. Phys.* 2006, 8, 1057-1065.
 32. F. Weigend and R. Ahlrichs, *Phys. Chem. Chem. Phys.* 2005, 7, 3297-3305.
 33. J. Frau and D. Glossman-Mitnik, *Theor. Chem. Acc.* 2018, 137, 1-10.
 34. S. Paranthaman, J. Moon, J. Kim, D. E. Kim and T. K. Kim, *J. Phys. Chem. A.* 2016, 120, 2128-2134.
 35. H. Afeefy, J. Liebman, S. Stein, Neutral thermochemical data. In P. Linstrom, W. Mallard, (eds.) NIST Chemistry WebBook, NIST Standard Reference Database Number. 69 (National Institute of Standards and Technology, Gaithersburg MD, USA, **2010**)
 36. AIMAll (Version 17.11.14), Todd A. Keith, TK Gristmill Software, Overland Park KS, USA, 2017 (aim.tk gristmill.com).
 37. J. K. Nørskov, J. Rossmeisl, A. Logadottir, L. Lindqvist, J. R. Kitchin, T. Bligaard and H. Jónsson, *J. Phys. Chem. B.* 2004, 108, 17886-17892.